ACS APPLIED MATERIALS & INTERFACES

Research Article

www.acsami.org

Large Scale and Orientation-Controllable Nanotip Structures on $CuInS_2$, $Cu(In,Ga)S_2$, $CuInSe_2$, and $Cu(In,Ga)Se_2$ by Low Energy Ion Beam Bombardment Process: Growth and Characterization

Yu-Ting Yen,[†] Yi-Chung Wang,[†] Yu-Ze Chen,[†] Hung-Wei Tsai,[†] Fan Hu,[†] Shih-Ming Lin,[†] Yi-Ju Chen,[†] Chih-Chung Lai,[†] Wenlong Liu,[†] Tsang-Hsiu Wang,[†] Hwen-Fen Hong,[‡] and Yu-Lun Chueh*,[†]

[†]Department of Materials Science and Engineering, National Tsing Hua University, Hsinchu City 30013, Taiwan

[‡]Institute of Nuclear Energy Research, No. 1000, Wenhua Road, Jiaan Village, Longtan Township, Taoyuan County 32546, Taiwan

Supporting Information

ABSTRACT: One-step facile methodology to create nanotip arrays on chalcopyrite materials (such as $CuInS_2$, $Cu(In,Ga)S_2$, $CuInSe_2$, and $Cu(In,Ga)Se_2$) via a low energy ion beam bombardment process has been demonstrated. The mechanism of formation for nanotip arrays has been proposed by sputtering yields of metals and reduction of metals induced by the ion beam bombardment process. The optical reflectance of these chalcopyrite nanotip arrays has been characterized by UV−vis spectrophotometer and the efficient light-trapping effect has been observed. Large scale (~4″) and high density (10^{10} tips/cm^2) of chalcopyrite nanotip arrays have been obtained by using low ion energy (< 1 kV), short processing duration (< 30 min), and template-free. Besides, orientation and length of these chalcopyrite nanotip arrays are controllable. Our results can be the guide for other nanostructured materials fabrication by ion sputtering and are available for industrial production as well.

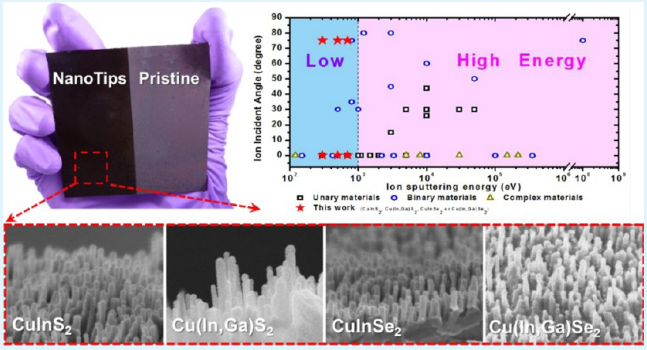

KEYWORDS: *sputtering etching, nano structure, ion bombardment, chalcopyrite*

1. INTRODUCTION

Creating a nanostructure in a large area with controlled manner raises specific interests on both academic and industrial fields. Among various approaches for manufacturing nanotechnology, ion sputtering has main advantages for creating a large scale and a highly uniform nanostructured surface in one step without a template. These advantages meet the demands for industrial processes. Some previous studies have reported that a nanostructured surface could be formed on unary (Si,[1−5] Ge,[1,6] Co,[7] Ag,[8] Ti,[9] Cu,[10] Sn,[11] Ta,[12] and C[13]), binary (InP,[14] InSb,[15] InAs,[16] GaAs,[17] GaSb,[18] WO_3,[19] CdS,[20] CaF_2,[21,22] KBr,[22] CdTe,[23] SiO_2,[24] and NiO[25]), minerals (mica[26]), tool steel,[27] and polymer (PTFE[28] and PMMA[29]) by controlling ion sputtering parameters precisely.

Conical arrays is well known as the best morphology to completely suppress Fresnel reflection at the surface due to a concept of gradual refractive index that has been theoretically and experimentally demonstrated by several research groups with tapered or vertically conical-shaped structures.[30,31] However, most of them need multiple processes, which are lower down throughput and yield, thereby raising the cost. Owing to harsh and complicate processes, very few methodologies for chalcopyrite nanostructure over zero-dimensional have been reported as well as vertical aligned chalcopyrite nanostructures.[32−35] In this regard, we propose a novel process for creating vertical aligned nanotip arrays (NTRs) on the surface of $CuInS_2$, $Cu(In,Ga)S_2$, $CuInSe_2$, and $Cu(In,Ga)Se_2$ films by the low energy ion beam bombardment process. For the proposed process, an ion beam with low kinetic energy was used for ternary and quaternary materials systems. NTRs with specific orientation and length were formed on a series of four chalcopyrites in a controlled manner. Surface morphology, density, and formation mechanisms of these chalcopyrites were analyzed and reported in detail. In addition, a ~4″ $Cu(In,Ga)Se_2$ sample was reported for a demonstration of scalability. Our results can be a guide for practical engineering developments because they are fast, in-line, and template-free.

2. EXPERIMENTAL SECTION

2.1. Preparation of $CuInS_2$, $Cu(In,Ga)S_2$, $CuInSe_2$, and $Cu(In,Ga)Se_2$ Thin Films. All chalcopyrites studied in this work were prepared by a two-step process with sulphurization or selenization processes depending on the final product. The precursor films of Cu/In and Cu/In/Ga layers were first deposited by physical vapor deposition onto a soda-lime glass (SLG, 2 × 2 cm) substrate which was coated by molybdenum. Then, a secondary sulphurization or selenization process

Received: February 26, 2014
Accepted: May 6, 2014
Published: May 6, 2014

   dx.doi.org/10.1021/am501161j | ACS Appl. Mater. Interfaces 2014, 6, 8327−8336

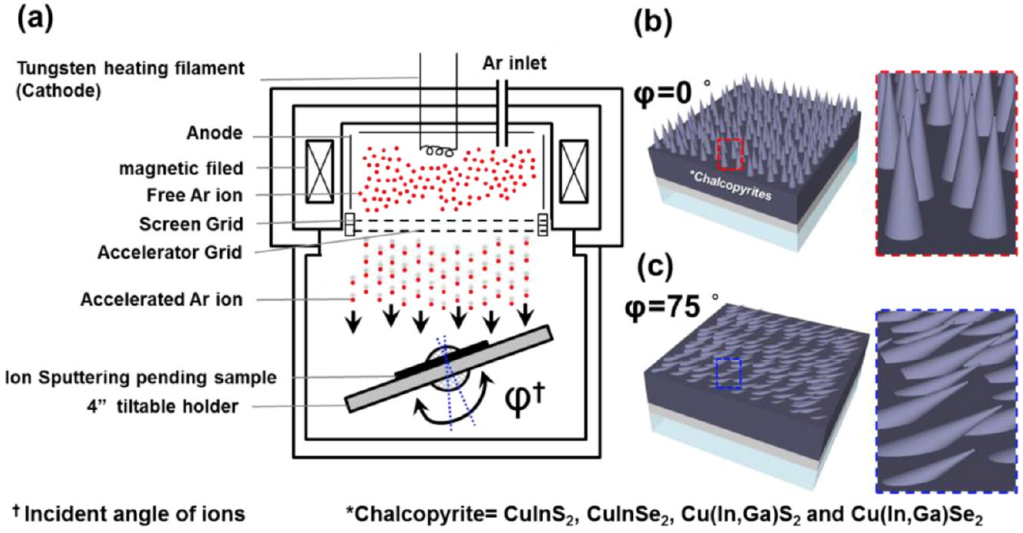

Figure 1. (a) Schematic illustration of main experimental process for fabrication nanotip arrays onto chalcopyrite materials. The orientation of NTRs can be tailored by simple change of the ion incident angle, φ (respect to surface normal). In this work, (b) $\varphi = 0°$ and (c) 75° has been demonstrated on four series of chalcopyrites.

was followed. The detailed procedures of preparation four chalcopyrite thin films are listed as follows.

2.1.1. Preparation of $CuInS_2$ Film. The $CuInS_2$ film was carried out by an electron beam evaporation system, which accommodated two separate targets (Cu and In). A multilayer (Cu/In/Cu/In) with thicknesses of 90 and 210 nm for Cu and In were deposited on the SLG substrate as shown in Supporting Information (SI) Figure S1a.

2.1.2. Preparation of $CuInSe_2$ Film. The $CuInSe_2$ thin film is identical with the process of fabrication $CuInS_2$ thin film except for the vapor source and the heating thermal profile.

2.1.3. Preparation of $Cu(In,Ga)S_2$ Film. Deposition of precursor films was carried out in a magnetic sputtering system, which accommodated with two separate targets (Cu/Ga and In). A 10-layer of CuGa/In with thickness of ~600 nm was deposited on the SLG substrate as shown in SI Figure S1b Then, the sulphurization process of the CuGa/In stack precursor was identical as $CuInS_2$ except the weight of sulphur was fixed at 60 mg.

2.1.4. Preparation of $Cu(In,Ga)Se_2$ Film. The $Cu(In,Ga)Se_2$ thin film has the identical process for fabrication $Cu(In,Ga)S_2$ thin film except for the vapor source and the heating thermal profile. The precursor with a 10-layer CuGa/In was selenized by selenium of 150 mg at 923 K for 20 min, and the heating rate was 75 K/min.

2.2. Sulphurization/Selenization Processes. Sulphurization/selenization process was carried out at a close-spaced graphite container, which is a push-pull rod equipped diffusion furnace. The close-spaced graphite container contains two separated rooms for a precursor sample and S/Se powder, which over-pressure of S/Se vapors are provided during the sulphurization/selenization process. The scheme of graphite container was depicted in SI Figure S2a. The graphite container with a precursor sample and 1.0/150 mg of S/Se powder were loaded into a quartz-tube diffusion furnace and were evacuated subsequently under 6.67×10^{-1} Pa by a mechanical rotary pump. Then, ambient gas (H_2 (25%) and N_2 (75%) in volume) was pumped into the quartz-tube and raised the pressure up to 8.00×10^3 Pa. A completed fabrication process for a $CuInS_2$ thin film was carried out by a heating process as shown in SI Figure S2b. For the selenization process, a Cu/In stack precursor sample was carried out with selenium of 150 mg at 773 K for 20 min, and the heating rate was 75 K/min from 298 to 773 K.

2.3. Formation of $CuInS_2$, $Cu(In,Ga)S_2$, $CuInSe_2$, and $Cu(In,Ga)Se_2$ Nanostructure Arrays by Ion Beam Bombardment Process. All chalcopyrite materials were processed by an ion beam etcher (Roth and Rau Unilab) with main characteristic of 0–90° adjustable ion incident angle, stage cooling, and substrate rotation to obtain nanotip arrays. The working window of beam energy, ion current, and ion current density are 0.2–2 keV, maximum up to 50 mA and 10 mA/cm^2, respectively. The ion gun is Kaufman type with two grids system. All samples were loaded into chamber with pressure kept at 4.00×10^{-4} Pa. Ar was selected as ion source and pumped into the chamber with working pressures between 1.60×10^{-2} to 2.74×10^{-2} Pa. The extracted ions were passed through highly transparent hexagonal-holes graphite grid before bombardment of chalcopyrite specimens. Filament and cathode current were fixed at 3.85 and 0.76 A, respectively. Beam and accelerator currents were set as 50 and 1 mA, respectively, with the accelerator voltage from 300 to 700 V.

2.4. Measurements and Characterization. Powder X-ray Diffraction (XRD) was conducted by a Shimadzu XRD-6000 X-ray spectrometer under irradiation of mono-chrome Cu–Kα ($\lambda \sim 1.54$ Å). Raman spectroscopy was acquired at room temperature with a micro-Raman spectrometer (Horiba Jobin-Yvon HR 800 UV) equipped with a liquid nitrogen cooled silicon CCD (Symphony-solo) in backscattering configuration with excitation wavelength as 632.8 nm. Morphology, nanostructure, and elemental compositions of chalcopyrite films were obtained by field emission scanning electron microscopy (FESEM by JEOL, JSE-6500F, and Hitachi, SU8000) and high resolution transmission electron microscopy (HR-TEM by JEOL, JEM-3000F FEGTEM, 300 kV) with attached accessory of Energy Dispersive Spectroscopy (EDS by INCA analysis system, Oxford Instruments). The specimens for TEM analysis were prepared by deposition of SiO_2 and Pt layers on top with thickness of 100 and 20 nm prior to focus ion beam (FIB) processing. Reflectance spectroscopy was acquired by the spectrophotometer (Hitachi, U-4100 UV–visible–NIR Spectrophotometer). X-ray photoelectron spectroscopy was performed by PerkinElmer Phi 1600 ESCA system under calibration by a Pt upper layer. The accelerating voltage of argon plasma and beam current density in XPS analysis were set as 15 kV and 2.8×10^3A/m^2 (25 mA in 9 mm^2), respectively.

3. RESULTS AND DISCUSSION

As can be seen in Figure 1, chalcopyrite films were loaded into a vacuum chamber and equipped with water-cooling system (Supporting Information for detailed fabrication of $CuInS_2$, $Cu(In,Ga)S_2$, $CuInSe_2$, and $Cu(In,Ga)Se_2$ thin films). Argon was used as an ion source gas, and the argon ions were screened and accelerated via two graphite grids (Figure 1a). The argon ions were screened and accelerated via collimated with a uniform sputter energy distribution. The ions were irradiated onto the chalcopyrite film with angle and length of chalcopyrite NTRs could be precisely controlled by controlling the stage, beam

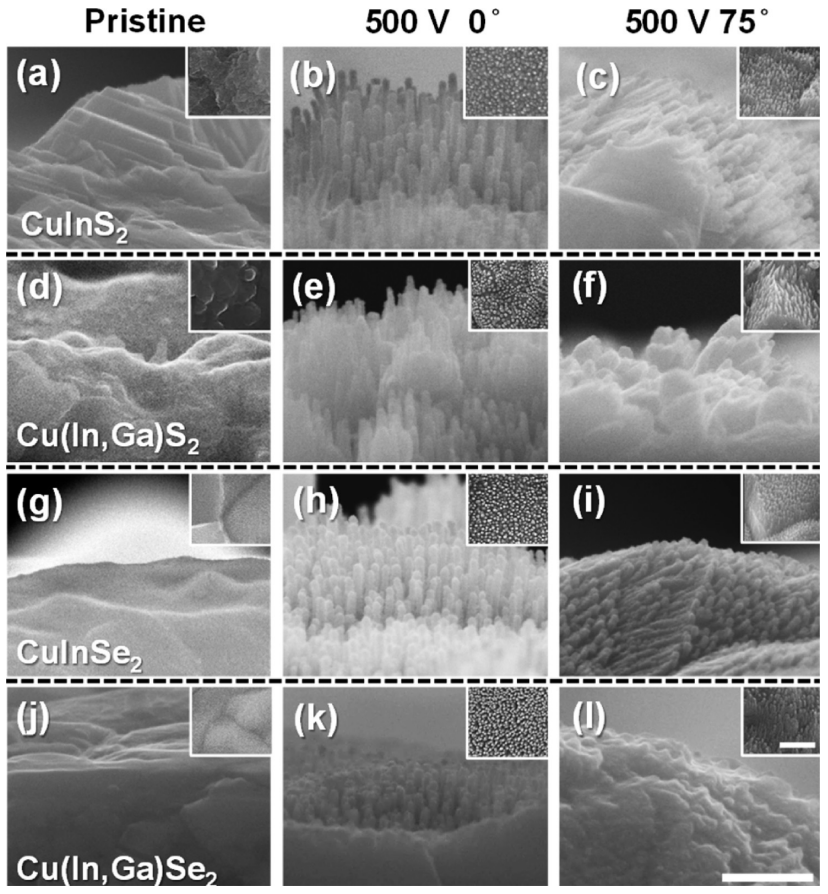

Figure 2. SEM cross-section images with top view of insets for chalcopyrite materials in various ion incident angles. Each row shows same chalcopyrite materials of (a–c) $CuInS_2$, (d–f) $Cu(In,Ga)S_2$, (g–i) $CuInSe_2$, and (j–l) $Cu(In,Ga)Se_2$ while each column represents (a, d, g, j) pristine, (b, e, h, k) normal (0°) incidence and (c, f, i, l) 75° of incidence. All specimens were bombarded by beam voltage of 500 V at 10 min. The scale bar is 300 and 500 nm for cross-section images and top view images in all insets, respectively.

voltage of accelerator, and ion sputtering time as shown in Figure 1b and c, respectively. Interestingly, we found that $CuInS_2$, $Cu(In,Ga)S_2$, $CuInSe_2$, and $Cu(In,Ga)Se_2$ could form NTRs by the single argon ion sputtering process and slightly varied in length and morphology. The detailed discussions are as follows.

Figure 2 shows scanning electron microscope (SEM) cross-section images of chalcopyrite materials in various incident angles by the low energy ion beam bombardment process under a beam voltage of 500 V for 10 min. In order to have reliable experimental results, pristine chalcopyrite films were used for comparison as shown in Figure 2a, d, g, and j, respectively. For the 0° of the incident angle with respect to surface normal, aligned NTRs on all chalcopyrite films, including $CuInS_2$, $Cu(In,Ga)S_2$, $CuInSe_2$ and $Cu(In,Ga)Se_2$ films, were observed after the low energy ion beam bombardment process, as shown in Figure 2b, e, h, and k, respectively. After changing incident angle from 0° to 75° with respect to surface normal, aligned NTRs with 15° were formed on the surface of films, as shown in Figure 2c, f, i, and l, respectively. Obviously, these NTRs are well aligned with the identical orientation. The prominent protuberance was found during sputtering time increased to 30 min. The corresponding SEM images were illustrated in Supporting Information (Figure S3m, n, o, and p).

To further investigate on the length dependence of chalcopyrite NTRs, the same batch of pristine films were used for the low energy ion beam bombardment process under applied voltages of 300, 500, and 700 V for 10 and 30 min, respectively. The cross-sectional SEM images of chalcopyrite materials in various energies are shown in Figure 3. Insets show the corresponding top-view SEM images. The lengths of these NTRs at various voltages and time are listed in Table 1. Obviously, the lengths of these NTRs were found in the order of $CuInS_2$ > $Cu(In,Ga)S_2$ > $CuInSe_2$ > $Cu(In,Ga)Se_2$ after the ion beam bombardment for 10 min. Similar observation can be observed on the applied voltage decreased from 700 to 300 V at the ion beam bombardment for 10 min or ion beam bombardment time increased from 10 to 30 min at all applied voltages. After the ion beam bombardment at applied voltage of 700 V for 30 min, a plateau of NTRs is formed instead of a tip. The breakage of NTRs is most likely induced by overdose of ion sputtering (SI Figure S3c, f, i, and l), which further hinder length increment of the NTRs. Furthermore, densities of NTRs from all chalcopyrite-based materials were found to be $\sim 3-4 \times 10^{10}$ tip/cm^2 as shown in Table 2 despite different biases were applied, indicating that no dependent density of NTRs with the applied biases.

Raman spectra were used to shed light on phase formation and structure characterization of NTRs formed by four different films as shown in Figure 4a–d, respectively. In addition, the pristine films are used for comparison before and after the ion beam bombardment process. Peaks at 291, 174, 293, and 175 cm^{-1} were found for the pristine $CuInS_2$, $CuInSe_2$, $CuInGaS_2$, and $CuInGaSe_2$.[36−39] No additional peaks were observed after the formation of the NTRs with differently applied biases confirming

dx.doi.org/10.1021/am501161j | ACS Appl. Mater. Interfaces 2014, 6, 8327−8336

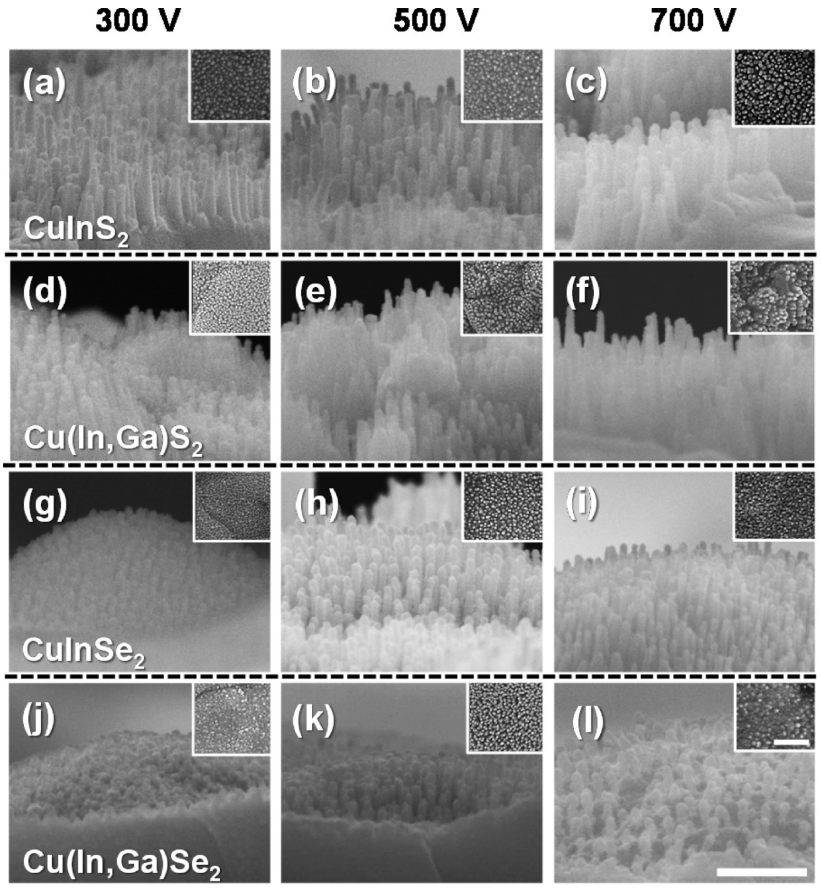

Figure 3. SEM cross-section images with top view of insets for chalcopyrite materials in various ion bombardment energies. Each row shows same chalcopyrite materials of (a–c) $CuInS_2$, (d–f) $Cu(In,Ga)S_2$, (g–i) $CuInSe_2$, and (j–l) $Cu(In,Ga)Se_2$ while each column represents ion bombardment under (a, d, g, j) 300 V, (b, e, h, k) 500 V, and (c, f, i, l) 700 V of beam voltage. All specimens encounter 10 min ion sputtering under normal incidence (0°, omitted for clarity) respect to surface normal. The scale bar is 300 and 500 nm for cross-section images and top view images in all insets, respectively.

Table 1. Chalcopyrite NTRs Length Distribution as Function of Sputtering Time and Beam Voltage

sputtering time (min)	beam voltage (Volt)	sputtered material NTRs length distribution (nm) (avg., stdev.)[a]			
		$CuInS_2$	$Cu(In,Ga)S_2$	$CuInSe_2$	$Cu(In,Ga)Se_2$
10	300	195(41)	91(9)	34(5)	29(5)
	500	208(16)	126(16)	131(35)	87(15)
	700	217(18)	186(22)	132(14)	81(13)
30	300	126(31)	87(22)	59(13)	33(6)
	500	158(20)	161(20)	132(21)	101(28)
	700	224(18)	208(60)	181(25)	97(21)

[a]avg. and stdev. are acronyms of "average" and "standard deviation" respectively.

Table 2. NTRs Density of Chalcopyrite Film after Ion Sputtering under Beam Voltage of 300, 500, and 700 V by 10 min

beam voltage (Volt)	sputtered material NTRs density (1×10^{10} NTRs/cm^2)			
	$CuInS_2$	$Cu(In,Ga)S_2$	$CuInSe_2$	$Cu(In,Ga)Se_2$
300	3.36	4.69	4.96	3.09
500	3.47	4.37	4.00	4.27
700	3.25	3.47	3.84	2.77

and no phase had been changed after the formation of the NTRs. The results are also consistent with X-ray diffraction spectra where all phases are the indexed belonging to $CuInS_2$, $CuInSe_2$, $CuInGaS_2$, and $CuInGaSe_2$ phases, respectively (SI Figure S4). Moreover, high-resolution TEM (HRTEM) and energy dispersive X-ray spectroscopy (EDS) have been used to further examination for the phase formation of NTRs after the ion beam bombardment process. Figure 5a, c, e, and g show the TEM images of $CuInS_2$, $CuInGaS_2$, $CuInSe_2$, and $CuInGaSe_2$ thin films without the ion beam bombardment process while Figure 5b, d, f, and h show the TEM images of $CuInS_2$, $CuInGaS_2$, $CuInSe_2$, and $CuInGaSe_2$ thin films after the ion beam bombardment process with accelerated bias of 700 V for 10 min. Obviously, lengths distribution of NTRS for $CuInS_2$, $CuInGaS_2$, $CuInSe_2$, and $CuInGaSe_2$ are found to be 203, 193, 102, and 58 nm, respectively and the lengths are in the order of $CuInS_2$ > $CuInGaS_2$ > $CuInSe_2$ > $CuInGaSe_2$, which are consistent with SEM results. Note that the statistic variation may come from the few samples of TEM images. The correlations between elemental compositions and vertical depth profiles of NTRs were extracted and plotted in Table 3, Table 4, and SI Figure S5. Compared to pristine films, the elemental distribution in NTRs is obviously dispersive, especially for copper (Cu), sulfur (S), and selenium (Se). Note that copper concentrations in these chalcopyrite NTRs are relatively higher at the top of tip and become convergent with the concentration of the bulk at bottom of the tip as shown in SI Figure S5 while In, S, or Se are depleted. In the

dx.doi.org/10.1021/am501161j | ACS Appl. Mater. Interfaces 2014, 6, 8327–8336

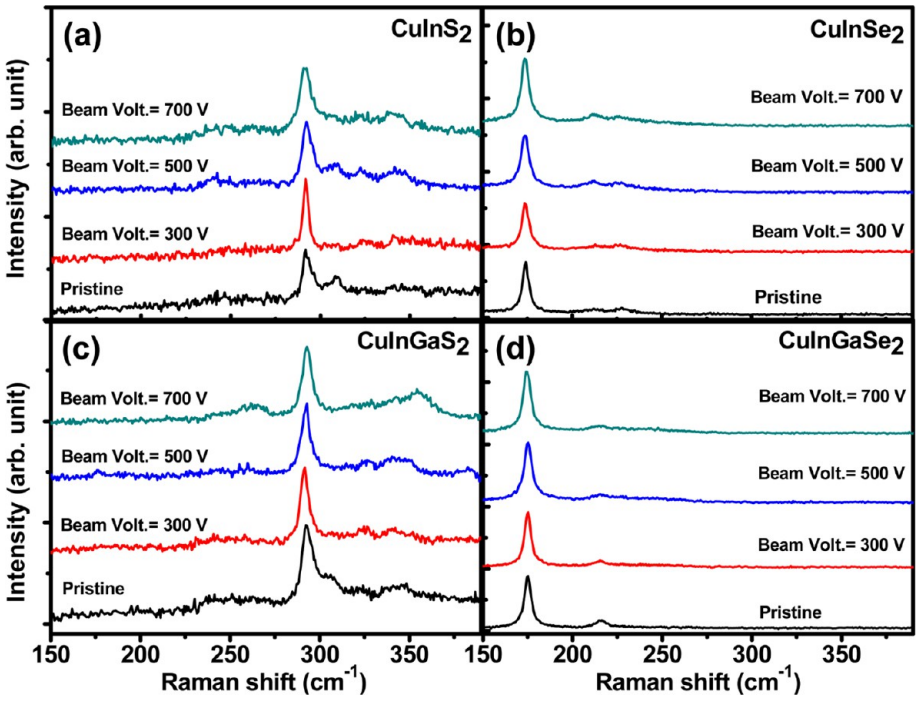

Figure 4. Raman spectra of pristine and nanotip arrays of (a) $CuInS_2$, (b) $CuInSe_2$, (c) $Cu(In,Ga)S_2$, and (d) $Cu(In,Ga)Se_2$ under different ion bombardment energy.

bulk film matrix, concentrations of Cu are decreased and concentrations of In, S, or Se are gradually increased. In addition, crystallinity of NTRs shows a single crystal feature confirmed by selected diffraction pattern before and after the ion bombardment process (SI Figure S6).

For the ion beam bombardment process, sputtering yield is one of critical factors to determine the final compositions of materials. The theory of Bradley−Harper has been widely used to interpret surface patterns induced by ion beam.[40−42] Due to the sputtering yields of Se, S, In, Ga, and Cu to be 5.2, 3.7, 2.1,1.6, and 1.8 atoms/ion with ion energy of 500 V at 0° incidence respectively, compositions of NTRs are different from the pristine chalcopyrite films.[43] The lowest sputtering yield and rich concentration in chalcopyrites result in Cu with the lowest milling rate compared to that of Se, S, Ga, and In, respectively. This is why Cu has found to be accumulated on the top of NTRs. After the ion bombardment process, the anisotropic etching process is needed to be taken into account. To shed light on the different sputtering yields, X-ray photoelectron spectroscopy (XPS) has been used to analyze bonding information on $CuInS_2$ NTRs. A function of depth profile (vertical distance along the surface of the NTRs, SI Figure S7) as a representative case is shown in Figure 6a, and a Cu $2p_{3/2}$ peak located at approximately 932.2 eV is detected.[44−46] Obviously, the peak shifts to a low binding energy along the vertical profile of NTRs, as shown in Figure 6b, suggesting that Cu atoms along the upper-tip region have less "bonding" with surrounding elements, namely reduction process. This is consistent with some previous studies reported that metal oxides were reduced by ions during the ion bombardment process.[19,47−49] It can be understood that similar results can be found on both metal sulfides and metal selenides because sulphur and selenium are in a same group and have a similar valence electron structure. A mechanism for formation of chalcopyrite NTRs is proposed, which is based on ions induced reduction process of metal oxides and curvature disparities of the surface, yielding different sputtering yields for different elements as shown in Figure 6c. Initially, high energy argon ions are accelerated and bombarded on a surface of a chalcopyrite film (Figure 6c1). Surface curvature dependent low sputtering yield and low oxidation state of metal ions result in uneven element distributions on the surface of chalcopyrite films, which will act as nucleation sites for the formation of the NTRs (Figure 6c2). In addition, Cu^+ were reduced to Cu atoms segregated on the surface of the chalcopyrite thin film. This is why metal (Cu) rich could be observed, which is consistent with TEM/EDS results. These high stoichiometry and low sputtering yield of coppers in a chalcopyrite film can serve as an ultrathin mask layer, which has higher milling resistance than other regions during the ion beam bombardment process (Figure 6c3). Finally, copper rich NTRs were formed anisotropically (Figure 6c4). It can be understood that lengths in the order of $CuInS_2$ > $CuInGaS_2$ > $CuInSe_2$ > $CuInGaSe_2$ are due to the disparity of Standard Gibbs free energy of formation and melting point. Because of incorporation of Ga into $CuInS_2$ or $CuInSe_2$, it results in increasing the Standard Gibbs free energy of formation of the species.[50] It means that the more stable compound require more energy to etch into nanostructures.[19] Therefore, under identical condition of ion sputtering, the length distribution should be (without Ga) > Ga-incorporated (i.e., $CuInS_2$ > $CuInGaS_2$ and $CuInSe_2$ > $CuInGaSe_2$). Because surface energy needs to be taken into account when conducting the ion bombardment process, surface energy tends to flatten the surface, which easily occurs on low melting point materials. The melting point of sulfides[51] are greater than selenides,[52] so the lengths of NTRs turns out selenides < sulfides, which consequently results in the length distribution of $CuInS_2$ > $CuInGaS_2$ > $CuInSe_2$ > $CuInGaSe_2$.

Nanostructured morphologies have been shown to possess a refractive index matching with air that significantly suppresses light reflection larger than pristine film structure over the whole spectrum.[30] UV−vis spectrophotometer has been used to have a better understanding of reflectance behaviors on these chalcopyrite NTRs. The reflectance spectra of these chalcopyrite

dx.doi.org/10.1021/am501161j | ACS Appl. Mater. Interfaces 2014, 6, 8327−8336

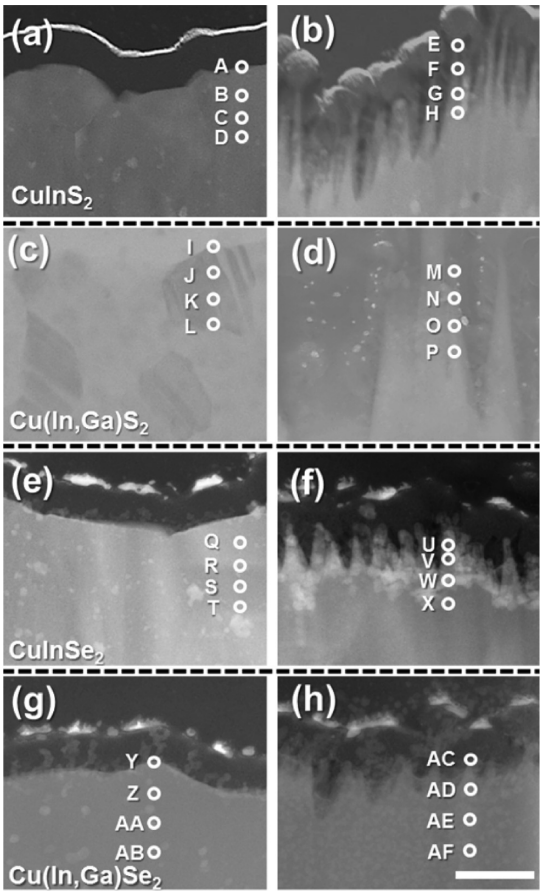

Figure 5. TEM images of pristine and nanotip arrays of chalcopyrite materials with EDS quantitative line scan points corresponding to SI Figure S5 and Tables 3 and 4. Each row shows same chalcopyrite materials of (a, b) $CuInS_2$, (c, d) $Cu(In,Ga)S_2$, (e, f) $CuInSe_2$ and (g, h) $Cu(In,Ga)Se_2$ while each column represents (a, c, e, g) pristine and (b, d, f, h) chalcopyrite NTRs. Note that all specimens are deposited by SiO_2 and Pt prior to FIB processing. The scale bar is 200 nm.

NTRs with differently accelerated voltages from 300 to 700 V are shown in Figure 7. Clearly, anti-reflection effects are evident. Insets show that surface of films goes darker as the accelerated voltage (i.e. length of NTRs) increases, especially distinguished in the visible light range. As can be seen in Figure 2 insets, the spatial distance between NTRs in these chalcopyrites are all shorter than 100 nm, which are distinctly shorter than the wavelength in visible range (390−700 nm). According to the efficient light-trapping effect, the incident light will be trapped by a large area nanostructure matrix. This character results in an important performance of optoelectronic devices for these chalcopyrite materials. By fabricating nanotips onto chalcopyrites in a controlled manner, benefits for self-cleaning, mechanical robustness can be expected.[53] Moreover, the facile process of this approach can be applied for further developments and design of complicated nanostructures for efficient light absorption and electric generation to optimization of photovoltaic devices.[54]

A plot of ion bombardment energy and incident angle versus various materials for the ion sputtering process is depicted in Figure 8. Our process undergoes in low beam voltages (300−700 V) and in a short process time (10−30 min), compared to other cases of nanostructure formed by the ion bombard process. In addition, our process is a low-cost methodology for fabrication of chalcopyrite nanostructures; besides, the orientations of these

Table 3. Line Scan Quantitative EDS Results of $CuInS_2$ and $Cu(In,Ga)S_2$ Corresponding to Analysis Points in Figure 5

material	pristine or NTRs	analyzed point	composition (at. %) Cu	In/Ga	S
$CuInS_2$	pristine	A	28.0	46.1	25.9
		B	22.9	53.1	24.0
		C	20.1	53.1	26.8
		D	20.3	49.6	30.1
	NTRs	E	40.9	42.0	17.1
		F	70.3	19.0	10.7
		G	26.9	51.2	21.9
		H	27.8	46.2	26.0
$Cu(In,Ga)S_2$	pristine	I	24.2	50.2/0.4	25.2
		J	22.3	51.4/1.1	25.2
		K	22.5	52.3/0.6	24.6
		L	24.5	50.4/1.6	23.5
	NTRs	M	36.9	26.5/15.4	21.2
		N	24.5	51.8/0.9	22.8
		O	24.1	48.9/2.1	24.9
		P	24.6	48.6/0.0	26.8

Table 4. Line Scan Quantitative EDS Rsults of $CuInSe_2$ and $Cu(In,Ga)Se_2$ Correspond to Analysis Points in Figure 5

material	pristine or NTRs	analyzed point	composition (at. %) Cu	In/Ga	Se
$CuInSe_2$	pristine	Q	18.0	36.1	45.9
		R	13.3	43.0	43.7
		S	14.5	40.0	45.6
		T	14.4	45.8	39.8
	NTRs	U	59.2	20.2	20.6
		V	22.3	60.0	17.7
		W	17.2	36.0	46.9
		X	21.3	36.8	41.9
$Cu(In,Ga)Se_2$	pristine	Y	13.2	36.4/4.1	46.3
		Z	15.1	34.5/4.2	46.2
		AA	13.6	39.8/4.5	42.2
		AB	14.0	36.8/4.6	44.6
	NTRs	AC	26.2	23.9/8.5	41.4
		AD	19.5	29.8/6.2	44.6
		AE	15.2	30.2/5.4	49.2
		AF	16.9	29.2/7.4	46.6

chalcopyrite nanostructures are controllable. A large scale and a rapid process are essentials for industrial applications. To shed light on larger scalability of the ion bombardment process, a ~4 inch with uniform NTRs on surface of $Cu(In,Ga)Se_2$ film has been successfully demonstrated by using the ion bombard process as shown in inset of Figure 8. Our results show that chalcopyrite nanostructure fabricated by ion sputtering has a great potential for industrial production lines due to low cost and short process time. Besides, our fabrication process is able to be implemented into other material systems such as InAs, Cu_2S, or Cu_2ZnSnS_4 as well.

dx.doi.org/10.1021/am501161j | ACS Appl. Mater. Interfaces 2014, 6, 8327−8336

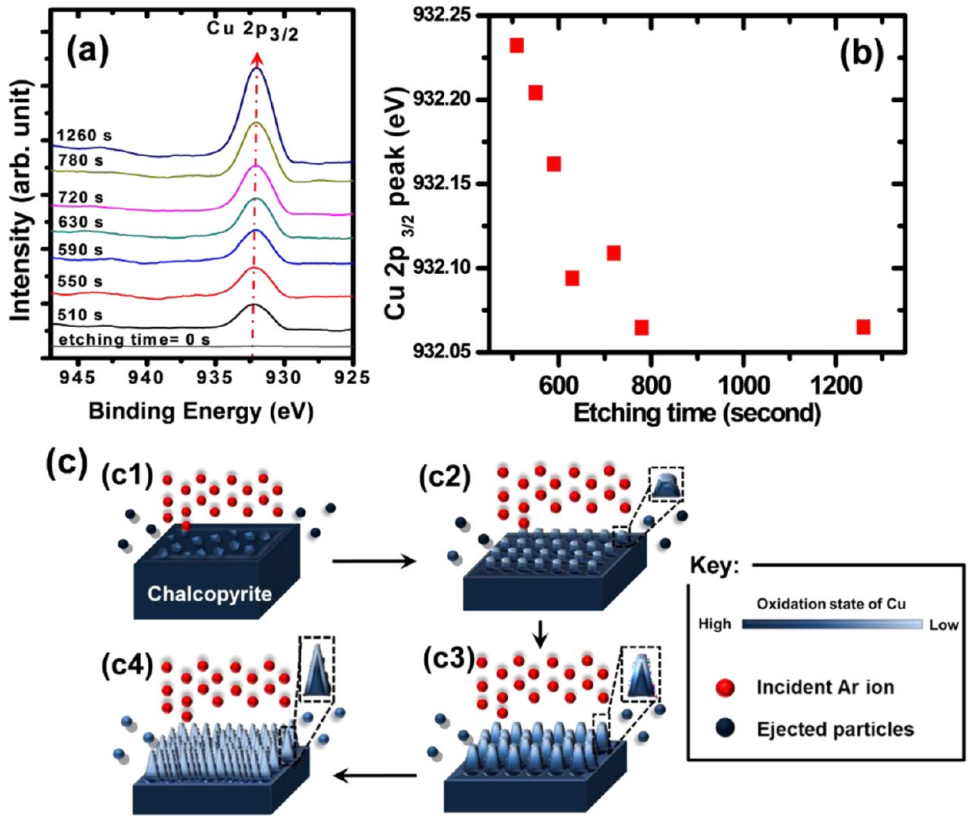

Figure 6. (a) XPS spectrum of Cu $2p_{3/2}$ from $CuInS_2$ nanotip arrays specimen. (b) Cu $2p_{3/2}$ peak position as a function of analysis point corresponding to part a. (c) Illustration of evolution of ion sputtering induced nanotip arrays based on proposed mechanism in the text. In consequence of (c1) energetic Ar^+ ion bombard on chalcopyrite surface, (c2) disparity of sputter yield create uneven element distribution, (c3) ion sputtering induced reduction of Cu^+ take place result Cu rich surface and served as ultra-thin masking layer to form (c4) Cu rich NTRs anisotropically.

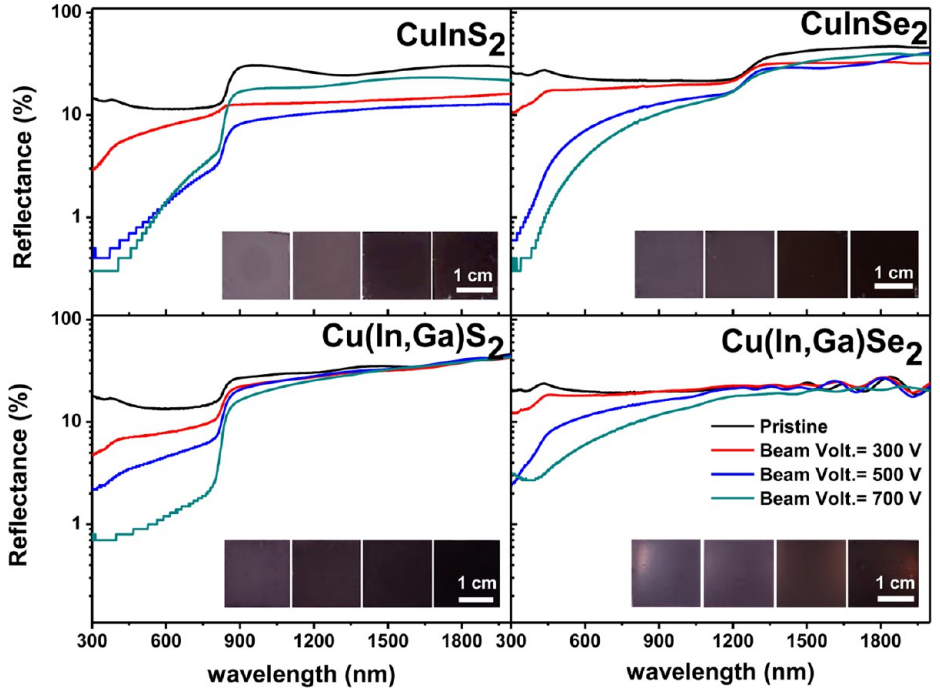

Figure 7. Reflectance spectra with specimen photos of insets for chalcopyrite materials encounter 10 min ion sputtering under various ion bombardment energies. The inset photos are specimens bombarded under beam voltage of 0, 300, 500, and 700 V from left to the right, respectively.

dx.doi.org/10.1021/am501161j | ACS Appl. Mater. Interfaces 2014, 6, 8327−8336

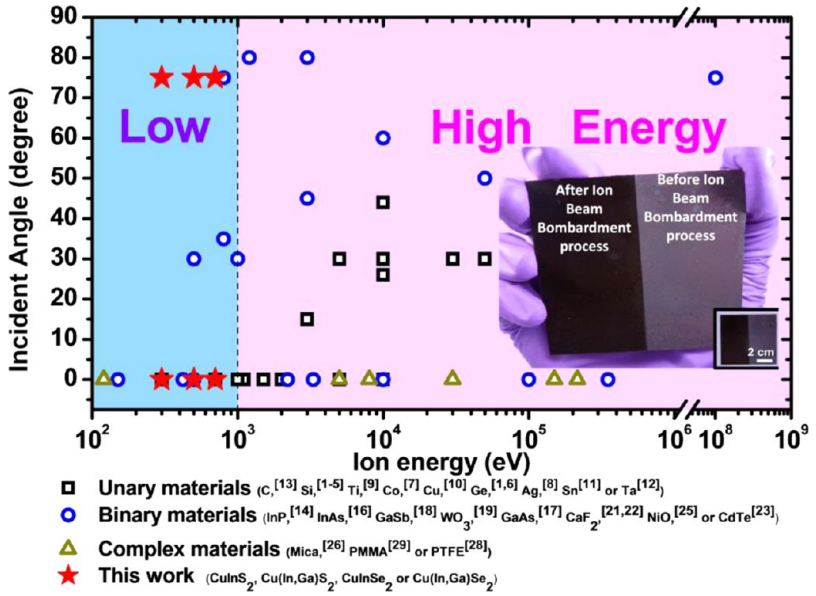

Figure 8. Previous works of ion sputtering induced nanostructures toward various materials as a function of ion bombardment energy and incident angle, with inset of a ~4″ specimen (in diagonal) of $Cu(In,Ga)Se_2$ with half nanotip arrays and pristine for demonstration the large scale of ion sputtering induced nanostructure process. Note that this work requires less energy and creates nanostructures under various ion incident angles.

4. CONCLUSIONS

We have successfully demonstrated a large-area and highly uniform nanostructures of chalcopyrite materials fabricated by ion sputtering. Our process provides a lot of advantageous for chalcopyrite nanostructure fabrication, such as controllable tilting angle and length, template free, high reproducibility and low energy required. Our results show that NTRs on chalcopyrite materials with an intact phase has been found. The anisotropic ion erosion phenomena have been observed, suggesting that they are resulted from surface curvature dependent sputtering yield of metals and reduction of metals induced by ion sputtering. The remarkable light trapping effect has been observed due to nanostructured gradient refractive index. Our results can be the guide for other nanostructured materials fabrication by ion sputtering; moreover, our results are available for industrial production.

■ ASSOCIATED CONTENT

Supporting Information

SEM cross-section images of metal precursor layer stacks subject prior to sulphurization/selenization process for final product as $CuInS_2$ or $CuInSe_2$, $Cu(In,Ga)S_2$, and $Cu(In,Ga)Se_2$; schematic layout of close-spaced graphite container utilized for sulphurization or selenization and thermal profile for sulphurize or selenize precursor stack into chalcopyrite; SEM cross-section images of chalcopyrite materials experience ion sputtering under different ion bombardment energy and incident angle respect to surface normal; XRD results of pristine and nanotip arrays of $CuInS_2$, $CuInSe_2$, $Cu(In,Ga)S_2$, and $Cu(In,Ga)Se_2$ under different ion bombardment energy; line scan of quantitative analysis obtained from an energy dispersive spectrometer (EDS); diffraction patterns of $CuInSe_2$ pristine and NTR(after Ar sputtering); schematic layout of XPS analysis path. This material is available free of charge via the Internet http://pubs.acs.org/.

■ AUTHOR INFORMATION

Corresponding Author

*Tel.: +886 3 5715131 ext 33965. Email: ylchueh@mx.nthu.edu.tw.

Notes

The authors declare no competing financial interest.

■ ACKNOWLEDGMENTS

The research was supported by the Ministry of Science and Technology through Grant No. 101-2112-M-007-015-MY3, 101-2218-E-007-009-MY3, 102-2633-M-007-002, and the National Tsing Hua University through Grant No. 102N2022E1. Y.L. Chueh greatly appreciates the use of facility at CNMM, National Tsing Hua University through Grant No. 102N2744E1.

■ REFERENCES

(1) Ziberi, B.; Cornejo, M.; Frost, F.; Rauschenbach, B. Highly Ordered Nanopatterns on Ge and Si Surfaces by Ion Beam Sputtering. *J. Phys.: Condens. Matter* **2009**, *21*, 224003−17.

(2) Miyamoto, I.; Yanagimoto, K.; Pahlovy, S. A.; Mahmud, S. F. Changes of Ripple Morphology of Cleaved Si Surface by Low-Energy Ar^+ Ion Beam Sputtering. *Int. J. Nanosci.* **2011**, *10*, 495−499.

(3) Ziberi, B.; Frost, F.; Rauschenbach, B.; Hoche, T. Highly Ordered Self-Organized Dot Patterns on Si Surfaces by Low-Energy Ion-Beam Erosion. *Appl. Phys. Lett.* **2005**, *87*, 033113−3.

(4) Munoz-Garcia, J.; Gago, R.; Cuerno, R.; Sanchez-Garcia, J. A.; Redondo-Cubero, A.; Castro, M.; Vazquez, L. Independence of Interrupted Coarsening on Initial System Order: Ion-Beam Nanopatterning of Amorphous versus Crystalline Silicon Targets. *J. Phys.: Condens. Matter* **2012**, *24*, 375302−8.

(5) Zhou, J.; Hildebrandt, M.; Lu, M. Self-Organized Antireflecting Nano-cone Arrays on Si (100) Induced by Ion Bombardment. *J. Appl. Phys.* **2011**, *109*, 053513−5.

(6) Wei, Q.; Zhou, X.; Joshi, B.; Chen, Y.; Li, K.-D.; Wei, Q.; Sun, K.; Wang, L. Self-Assembly of Ordered Semiconductor Nanoholes by Ion Beam Sputtering. *Adv. Mater.* **2009**, *21*, 2865−2869.

(7) Arranz, M. A.; José, M. C. Nanoscale Ripple Formation in Co/Si(100) Thin Films with Ar^+ Beam Etching. *J. Phys.: Conf. Ser.* **2010**, *200*, 072007−4.

(8) Rusponi, S.; Boragno, C.; Valbusa, U. Ripple Structure on Ag(110) Surface Induced by Ion Sputtering. *Phys. Rev. Lett.* **1997**, *78*, 2795−2798.
(9) Riedel, N.; Williams, J.; Popat, K. Ion Beam Etching Titanium for Enhanced Osteoblast Response. *J. Mater. Sci.* **2011**, *46*, 6087−6095.
(10) Reiche, R.; Hauffe, W. Pyramid Formation on A High Index Copper Bicrystal During Bombardment with 10 keV Argon and Krypton Ions. *Appl. Surf. Sci.* **2000**, *165*, 279−287.
(11) Qian, H. X.; Zhou, W.; Zeng, X. R. Dwell Time Dependent Morphological Transition and Sputtering Yield of Ion Sputtered Sn. *J. Phys. D: Appl. Phys.* **2010**, *43*, 345302−4.
(12) Medicherla, V. R. R.; Majumder, S.; Paramanik, D.; Varma, S. Formation of Self-Organized Ta Nano-structures by Argon Ion Sputtering of Ta Foil: XPS and AFM Study. *J. Electron Spectrosc. Relat. Phenom.* **2010**, *180*, 1−5.
(13) Habenicht, S.; Bolse, W.; Lieb, K. P.; Reimann, K.; Geyer, U. Nanometer Ripple Formation and Self-Affine Roughening of Ion-Beam-Eroded Graphite Surfaces. *Phys. Rev. B* **1999**, *60*, R2200−R2203.
(14) Frost, F.; Schindler, A.; Bigl, F. Roughness Evolution of Ion Sputtered Rotating InP Surfaces: Pattern Formation and Scaling Laws. *Phys. Rev. Lett.* **2000**, *85*, 4116−4119.
(15) Saeed, S. R.; Sinha, O. P.; Krok, F.; Zembok, T.; Pedrys, R.; Szymonski, M. Temperature-Dependent Surface Modification of InSb(001) Crystal by Low-Energy Ion Bombardment. *Nucl. Instrum. Methods Phys. Res., Sect. B* **2009**, *267*, 2752−2756.
(16) Ziberi, B.; Frost, F.; Tartz, M.; Neumann, H.; Rauschenbach, B. Importance of Ion Beam Parameters on Self-Organized Pattern Formation on Semiconductor Surfaces by Ion Beam Erosion. *Thin Solid Films* **2004**, *459*, 106−110.
(17) Kumar, T.; Kumar, M.; Gupta, G.; Pandey, R.; Verma, S.; Kanjilal, D. Role of Surface Composition in Morphological Evolution of GaAs Nano-Dots with Low-Energy Ion Irradiation. *Nanoscale Res. Lett.* **2012**, *7*, 552−8.
(18) Facsko, S.; Dekorsy, T.; Koerdt, C.; Trappe, C.; Kurz, H.; Vogt, A.; Hartnagel, H. L. Formation of Ordered Nanoscale Semiconductor Dots by Ion Sputtering. *Science* **1999**, *285*, 1551−1553.
(19) Xie, F. Y.; Gong, L.; Liu, X.; Tao, Y. T.; Zhang, W. H.; Chen, S. H.; Meng, H.; Chen, J. XPS Studies on Surface Reduction of Tungsten Oxide Nanowire Film by Ar^+ Bombardment. *J. Electron Spectrosc. Relat. Phenom.* **2012**, *185*, 112−118.
(20) Sulania, I.; Agarwal, D.; Tripathi, S. K.; Husain, M. Modifications on CdS Thin Films Due to Low-Energy Ion Bombardment. *Radiat. Eff. Defects Solids* **2011**, *167*, 59−68.
(21) El-Said, A. S.; Meissl, W.; Simon, M. C.; Crespo López-Urrutia, J. R.; Gebeshuber, I. C.; Lang, M.; Winter, H. P.; Ullrich, J.; Aumayr, F. Surface Nanostructures Induced by Slow Highly Charged Ions on CaF_2 Single Crystals. *Nucl. Instrum. Methods Phys. Res., Sect. B* **2007**, *256*, 346−349.
(22) Facsko, S.; Meissl, W.; Heller, R.; Wilhelm, R.; El-Said, A. S.; Kowarik, G.; Ritter, R.; Aumayr, F. Nanostructures Induced by Highly Charged Ions on CaF_2 and KBr. *J. Phys.: Conf. Ser.* **2009**, *194*, 012060−8.
(23) Shanmugan, S.; Mutharasu, D. An Effect of N^+ Ion Bombardment on the Properties of CdTe Thin Films. *Radiat. Phys. Chem.* **2012**, *81*, 201−207.
(24) Toma, A.; Buatier de Mongeot, F.; Buzio, R.; Firpo, G.; Bhattacharyya, S. R.; Boragno, C.; Valbusa, U. Ion Beam Erosion of Amorphous Materials: Evolution of Surface Morphology. *Nucl. Instrum. Methods Phys. Res., Sect. B* **2005**, *230*, 551−554.
(25) Chauhan, R. S.; Agarwal, D. C.; Kumar, S.; Khan, S. A.; Kabiraj, D.; Sulania, I.; Avasthi, D. K.; Bolse, W. Nano/Micro-structuring of Oxide Thin Film under SHI Irradiation. *Vacuum* **2011**, *86*, 96−100.
(26) Ritter, R.; Kowarik, G.; Meissl, W.; El-Said, A. S.; Maunoury, L.; Lebius, H.; Dufour, C.; Toulemonde, M.; Aumayr, F. Nanostructure Formation due to Impact of Highly Charged Ions on Mica. *Vacuum* **2010**, *84*, 1062−1065.
(27) Nakasa, K.; Zhang, Q. L.; Wang, R. G.; Kato, M. Nano-indentation Characteristics of Surface Layer with Fine Conical Protrusions Formed by Sputter Etching of W-Cr Tool Steel. *J. Jpn. Inst. Met.* **2009**, *73*, 870−877.
(28) Inoue, Y.; Yoshimura, Y.; Ikeda, Y.; Kohno, A. Ultra-hydrophobic Fluorine Polymer by Ar-Ion Bombardment. *Colloids Surf., B* **2000**, *19*, 257−261.
(29) Kaless, A.; Schulz, U.; Munzert, P.; Kaiser, N. Nano-Motheye Antireflection Pattern by Plasma Treatment of Polymers. *Surf. Coat. Technol.* **2005**, *200*, 58−61.
(30) Stavenga, D. G.; Foletti, S.; Palasantzas, G.; Arikawa, K. Light on the Moth-Eye Corneal Nipple Array of Butterflies. *Proc. R. Soc. B* **2006**, *273*, 661−667.
(31) Chattopadhyay, S.; Huang, Y. F.; Jen, Y. J.; Ganguly, A.; Chen, K. H.; Chen, L. C. Antireflecting and Photonic Nanostructures. *Mater. Sci. Eng., R* **2010**, *69*, 1−35.
(32) Hsin, C.-L.; Lee, W.-F.; Huang, C.-T.; Huang, C.-W.; Wu, W.-W.; Chen, L.-J. Growth of $CuInSe_2$ and In_2Se_3/$CuInSe_2$ Nano-heterostructures through Solid State Reactions. *Nano Lett.* **2011**, *11*, 4348−4351.
(33) Xu, J.; Lee, C.-S.; Tang, Y.-B.; Chen, X.; Chen, Z.-H.; Zhang, W.-J.; Lee, S.-T.; Zhang, W.; Yang, Z. Large-Scale Synthesis and Phase Transformation of CuSe, $CuInSe_2$, and $CuInSe_2$/$CuInS_2$ Core/Shell Nanowire Bundles. *ACS Nano* **2010**, *4*, 1845−1850.
(34) Peng, H.; Schoen, D. T.; Meister, S.; Zhang, X. F.; Cui, Y. Synthesis and Phase Transformation of In_2Se_3 and $CuInSe_2$ Nanowires. *J. Am. Chem. Soc.* **2006**, *129*, 34−35.
(35) Liu, C.-H.; Chen, C.-H.; Chen, S.-Y.; Yen, Y.-T.; Kuo, W.-C.; Liao, Y.-K.; Juang, J.-Y.; Kuo, H.-C.; Lai, C.-H.; Chen, L.-J.; Chueh, Y.-L. Large Scale Single-Crystal $Cu(In,Ga)Se_2$ Nanotip Arrays for High Efficiency Solar Cell. *Nano Lett.* **2011**, *11*, 4443−4448.
(36) Witte, W.; Kniese, R.; Eicke, A.; Powalla, M. Influence of the Ga Content on the Mo/$Cu(In,Ga)Se_2$ Interface Formation. *IEEE 4th World Conference on Photovoltaic Energy Conversion*; 2006; pp 553−556.
(37) Witte, W.; Kniese, R.; Powalla, M. Raman Investigations of $Cu(In,Ga)Se_2$ Thin Films with Various Copper Contents. *Thin Solid Films* **2008**, *517*, 867−869.
(38) Álvarez-García, J.; Marcos-Ruzafa, J.; Pérez-Rodríguez, A.; Romano-Rodríguez, A.; Morante, J. R.; Scheer, R. MicroRaman Scattering from Polycrystalline $CuInS_2$ Films: Structural Analysis. *Thin Solid Films* **2000**, *361−362*, 208−212.
(39) Oja, I.; Nanu, M.; Katerski, A.; Krunks, M.; Mere, A.; Raudoja, J.; Goossens, A. Crystal Quality Studies of $CuInS_2$ Films Prepared by Spray Pyrolysis. *Thin Solid Films* **2005**, *480−481*, 82−86.
(40) Bradley, R. M.; Harper, J. M. E. Theory of Ripple Topography Induced by Ion Bombardment. *J. Vac. Sci. Technol., A* **1988**, *6*, 2390−2395.
(41) Bradley, R. M.; Shipman, P. D. Spontaneous Pattern Formation Induced by Ion Bombardment of Binary Compounds. *Phys. Rev. Lett.* **2010**, *105*, 145501−4.
(42) Shipman, P. D.; Bradley, R. M. Theory of Nanoscale Pattern Formation Induced by Normal-Incidence Ion Bombardment of Binary Compounds. *Phys. Rev. B* **2011**, *84*, 085420−14.
(43) Seah, M. P.; Clifford, C. A.; Green, F. M.; Gilmore, I. S. An Accurate Semi-empirical Equation for Sputtering Yields I: For Argon Ions. *Surf. Interface Anal.* **2005**, *37*, 444−458.
(44) Schön, G. High Resolution Auger Electron Spectroscopy of Metallic Copper. *J. Electron Spectrosc. Relat. Phenom.* **1972**, *1*, 377−387.
(45) Schön, G. ESCA Studies of Cu, Cu_2O, and CuO. *Surf. Sci.* **1973**, *35*, 96−108.
(46) Strohmeier, B. R.; Levden, D. E.; Field, R. S.; Hercules, D. M. Surface Spectroscopic Characterization of $CuAl_2O_3$ Catalysts. *J. Catal.* **1985**, *94*, 514−530.
(47) Kim, K. S.; Baitinger, W. E.; Amy, J. W.; Winograd, N. ESCA Studies of Metal−Oxygen Surfaces Using Argon and Oxygen Ion-Bombardment. *J. Electron Spectrosc. Relat. Phenom.* **1974**, *5*, 351−367.
(48) Holm, R.; Storp, S. ESCA Investigations of Ion Beam Effects on Surfaces. *Phys. Scr.* **1977**, *16*, 442−447.
(49) Holm, R.; Storp, S. ESCA Studies on Changes in Surface Composition under Ion Bombardment. *Appl. Phys.* **1977**, *12*, 101−112.
(50) Cahen, D.; Noufi, R. Free Energies and Enthalpies of Possible Gas Phase and Surface Reactions for Preparation of $CuInSe_2$. *J. Phys. Chem. Solids* **1992**, *53*, 991−1005.

(51) Binsma, J. J. M.; Giling, L. J.; Bloem, J. Phase Relations in The System Cu_2S–In_2S_3. *J. Cryst. Growth* **1980**, *50*, 429–436.
(52) Tinoco, T.; Rincón, C.; Quintero, M.; Pérez, G. S. Phase Diagram and Optical Energy Gaps for $CuIn_yGa_{1-y}Se_2$ Alloys. *Phys. Status Solidi A* **1991**, *124*, 427–434.
(53) Liu, Y.; Das, A.; Lin, Z.; Cooper, I. B.; Rohatgi, A.; Wong, C. P. Hierarchical Robust Textured Structures for Large Scale Self-Cleaning Black Silicon Solar Cells. *Nano Energy* **2014**, *3*, 127–133.
(54) Kapadia, R.; Fan, Z.; Takei, K.; Javey, A. Nanopillar Photovoltaics: Materials, Processes, and Devices. *Nano Energy* **2012**, *1*, 132–144.